Nanoscale

PAPER

View Article Online
View Journal | View Issue

Cite this: *Nanoscale*, 2023, **15**, 12574

Sonoporation-assisted micelle delivery in subcutaneous glioma-bearing mice evaluated by PET/fluorescent bi-modal imaging†

Estelle Porret,‡[a] Stéphane Hoang,‡[b,c] Caroline Denis,[a] Eric Doris,[b] Martin Hrubý,[c] Anthony Novell,[a] Edmond Gravel *[b] and Charles Truillet *[a]

Tumor-specific drug delivery is a major challenge for the pharmaceutical industry. Nanocarrier systems have been widely investigated to increase and control drug delivery to the heterogeneous tumor microenvironment. Classically, the uptake of nanocarriers by solid tumor tissues is mainly mediated by the enhanced permeability and retention effect (EPR). This EPR effect depends on the tumor type, its location, the physicochemical properties of the carriers, and the blood perfusion of the tumoral lesions. The main goal of this study was to evaluate *in vivo* tumor uptake of micelle carriers, assisted by microbubble/ultrasound sonoporation. Micelles were tracked using bi-modal imaging techniques to precisely localize both the nanocarrier and its payload. Micelles were loaded with a near infrared fluorophore and radiolabeled with zirconium-89. Their pharmacokinetics, biodistribution and passive tumor targeting properties were evaluated in a subcutaneous glioblastoma (U-87 MG) mouse model using optical and PET imaging. Finally, accumulation and diffusion into the tumor micro-environment was investigated under microbubble-assisted sonoporation, which helped homogenize the delivery of the micelles. The *in vivo* experiments showed a good correlation between optical and PET images and demonstrated the stability of the micelles in biological media, their high and long-term retention in the tumors and their clearance through the hepato-biliary pathway. This study demonstrates that bi-modal imaging techniques are powerful tools for the development of new nanocarriers and that sonoporation is a promising method to homogenize nanomedicine delivery to tumors.

Received 3rd April 2023,
Accepted 9th July 2023

DOI: 10.1039/d3nr01539d

rsc.li/nanoscale

Introduction

Over the past 20 years, the development of nanoparticles (NPs) has generated great interest for a variety of medical applications, ranging from diagnosis to therapy, especially in the field of oncology.[1] The refinement of tumoral drug delivery has particularly benefited from the improvement of nanocarrier properties. Significant progress has been made to overcome drawbacks associated with hydrophobic anticancer drugs such as absorption issues, poor *in vivo* stability and rapid clearance.[2] Most of the nanoparticle formulations approved by the Food and Drug Administration and/or the European Medicines Agency related to drug delivery systems are based on nanocrystals, dendrimers, lipidic, polymeric, protein-based or inorganic NPs.[3] Adaptive nanoplatforms, that can combine diagnostic and therapeutic properties in a single object, are promising candidates for clinical translation.[4]

Among the different NPs, micelles present interesting features such as: (i) straightforward formation by self-assembly of amphiphilic unimers, (ii) high loading capacity of hydrophobic compounds into their core, and (iii) easy incorporation of reactive groups on their surface for further functionalization.[5,6] In addition, micelles can avoid rapid renal elimination as their size is above the kidney filtration threshold (*ca.* 6–8 nm).[7] In addition, their capture by the mononuclear phagocyte system (MPS), predominantly composed of resident macrophages in the spleen and liver, can be delayed by the addition of poly(ethylene glycol) chains at their surface in order to limit the opsonization phenomenon.[8,9] Micelles are thus capable of circulating long enough in the blood stream to passively accumulate in the tumor

[a]*Université Paris-Saclay, CEA, CNRS, Inserm, BioMaps, Service Hospitalier Frédéric Joliot, 4 place du général Leclerc, 91401 Orsay, France.*
E-mail: charles.truillet@cea.fr
[b]*Université Paris-Saclay, CEA, INRAE, Département Médicaments et Technologies pour la Santé (DMTS), SCBM, 91191 Gif-sur-Yvette, France.*
E-mail: edmond.gravel@cea.fr
[c]*Institute of Macromolecular Chemistry, Czech Academy of Sciences, Prague 162 06, Czech Republic*

†Electronic supplementary information (ESI) available. See DOI: https://doi.org/10.1039/d3nr01539d

‡These authors contributed equally to this work.

tissues.[5,9,10] It has to be noted that, currently, tens of percent of the Western population has anti-PEG antibodies due to everyday overuse of PEG-based detergents, which may lead to accelerated blood clearance phenomenon and decreased non-biofouling action of PEGylated nanospecies.[11]

Tumoral growth is accompanied by the development of abnormal tumor vasculature that can be somewhat leaky, with pore sizes between 300 and 1200 nm, and a perturbation of the lymphatic drainage. This phenomenon, known as the enhanced permeability and retention (EPR) effect, allows selective accumulation of NPs in cancer tissues at higher concentrations than in normal tissues.[12] However, the degree of blood vessel alteration can differ greatly based on cancer type and from one patient to the other.[13] Several studies suggests that nanocarriers reduce side-toxicity issues associated to chemotherapy but fail to improve treatment efficacy due to sub-optimal drug delivery and diffusion into the tumor.[9,14]

Functional biomedical imaging techniques such as positron emission tomography (PET) are promising methods to monitor the efficacy of drug delivery through EPR uptake[15] as the quantification of nanoparticles within the tumor heterogeneity has been established as a potent predictive biomarker for NP therapy.[16]

The development of more efficient delivery methods is required to increase local accumulation and retention of drugs at the desired site of action. One of the techniques currently explored to increase drug delivery in the tumor is sonoporation. It holds great promise for the improvement of gene[17] and drug delivery[18] to tumor tissues.[19] Sonoporation is a non-invasive technique, combining intravenous injection of microbubbles (μBs) with ultrasound (US). The resulting acoustic phenomenon enhances the permeability of vasculature and cell membranes through the formation of transitory nanopores and/or stimulates paracellular and transcellular pathways.[20] Although μBs combined with US are known to increase the therapeutic effectiveness of anticancer drugs such as doxorubicin[21–23] and irinotecan,[24] compared to US alone, this approach has so far not been explored to enhance the delivery of micelles to tumors.

In this context, we carefully designed core-polymerized micellar carriers to precisely control their physicochemical properties and bioavailability. These colloidal NPs were obtained by self-assembly of diacetylene (DA) amphiphiles that were further polymerized by UV irradiation in order to reduce their dynamic nature and improve their stability. By using this technique, it is possible to generate micelles with hydrodynamic diameters of approximately 10 nm and high drug-loading capacity, as demonstrated in previous investigations.[10,25–28,29]

In the present study, we developed a simple protocol for the synthesis of radiolabeled zirconium-89 ([^{89}Zr])-polymerized micelles. Micelles were loaded with a near infrared (NIR)-emitting fluorophore to mimic drug encapsulation and enable *in vivo* monitoring by optical imaging. This bi-modal PET/optical imaging allowed us to study both the micelles and their payload. We thus evaluated pharmacokinetics, biodistribution and accumulation of micelles mediated by the EPR effect in a subcutaneous glioblastoma (U-87 MG) mouse model using bi-modal imaging techniques. U-87 MG was chosen due to their high vascularization which is crucial for evaluating sonoporation efficacy.[30] We then investigated whether the administration of μBs combined with US tumor exposure could improve micelle accumulation, retention and diffusion into tumor tissues. Tumors were excised post imaging and subsequently analyzed using autoradiography and fluorescence microscopy to corroborate the *in vivo* PET/optical imaging results.

Results

Micelle synthesis, radiolabeling and stability

For this study, two different amphiphiles were designed and synthesized. Both molecules share the same lipophilic moiety, a C_{25} tail with a central diacetylene motive (DA), but differ in the nature of their polar region. The first amphiphile includes a poly(ethylene glycol) chain (PEG) as head-group (DA–PEG, Scheme 1), to convey biocompatibility and stealthiness[31] to the micelles, while the second amphiphile incorporates deferoxamine (DFO) (DA–DFO, Scheme 1), a ligand for [^{89}Zr] chelation,[32] to allow imaging by positron emission tomography.

Micelles were obtained from the co-assembly of DA–PEG and DA–DFO monomers at a ratio of 90:10 w/w. DA–PEG/DFO micelles were stabilized by UV-induced polymerization at 254 nm.[25,27,28] The polymerized pDA–PEG/DFO mixed-micelles were analyzed by dynamic light scattering (DLS) which showed a monodisperse population with a mean hydrodynamic dia-

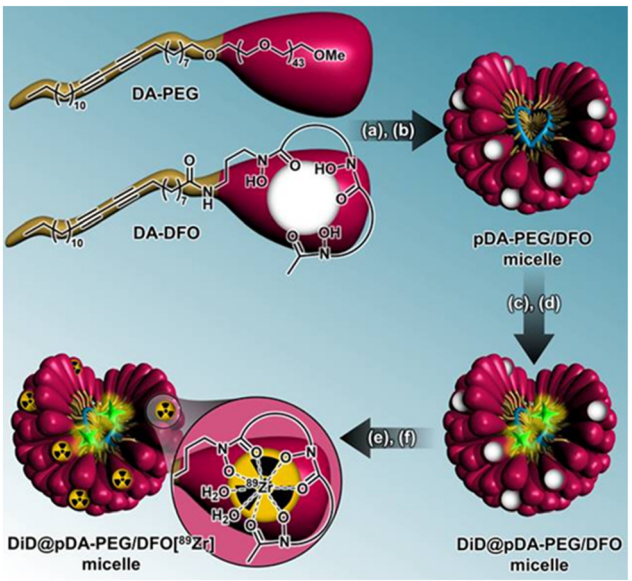

Scheme 1 Micelle synthesis steps with radiolabeling strategy. Step 1: (a) formation of micelles in aqueous solution (>CMC, pH 12) and (b) polymerization by UV irradiation (254 nm). Step 2: (c) DiD encapsulation (λ_{exc} ~ 645 nm, $\lambda_{em.}$ ~ 665 nm) and (d) pre-purification a PD-10 column at pH 7.8. Step 3: (e) radiolabeling of the micelles platform using ^{89}Zr and (f) post-purification *via* a PD-10 column and vivaspin.

meter of 8.4 nm (Fig. S1 and S2A†). The pDA–PEG/DFO micelles were then loaded with 0.8 wt% of fluorescent DiD dye before purification by size exclusion chromatography (PD-10 column, see Fig. S2B† for HPLC-UV characterization).[33] The fluorescence spectrum of DiD@pDA–PEG/DFO micelles in pH 7.0 PBS was recorded and showed a broad near infrared emission peak between 640 and 720 nm (λ_{exc} = 575 nm) with a maximum at 665 nm (Fig. S2C†), in agreement with the fluorescence properties of DiD.[34,35]

The DiD@pDA–PEG/DFO micelles were then radiolabeled with ^{89}Zr.[36,37] The radio-chromatogram of the ^{89}Zr-labelled micelles showed a sharp peak at 19 min (Fig. 1A) that corresponds to the reference peak of DiD@pDA–PEG/DFO detected by UV (Fig. S2B†). Radio-iTLC analyses highlight the importance of the purification step of the DFO-micelles in order to obtain a high radiochemical purity, superior to 99% (Fig. 1B and C, and Fig. S3†). During the radiochemical procedure, no leaching of DiD was observed. The radioactive signal of DiD@pDA–PEG/DFO[^{89}Zr] micelles is colocalized with their fluorescent signal (Fig. 1C and D).

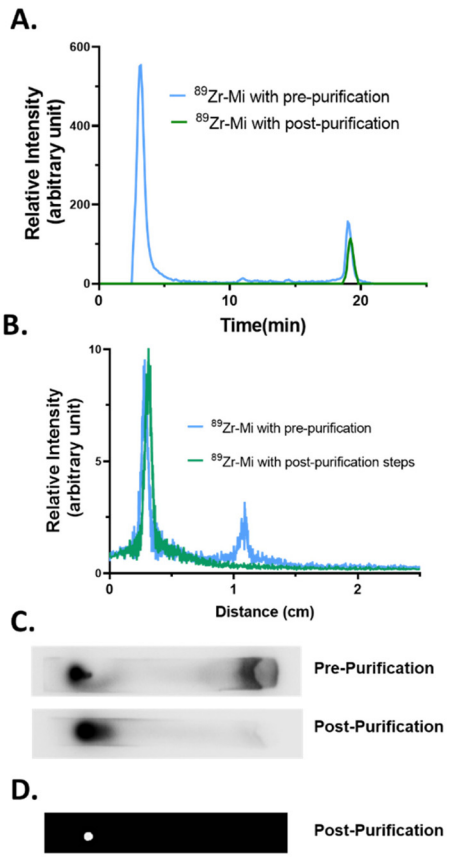

Fig. 1 Characterization of DiD@pDA–PEG/DFO[^{89}Zr] micelles. (A) Radio-HPLC chromatograms after ^{89}Zr radiolabeling of the DiD@pDA–PEG/DFO micelles pre-purification (blue) or post purification (green). (B) Radio-TLC chromatograms, (C) dots autoradiography and (D) fluorescence (λ_{exc} = 665 nm) of the previous ^{89}Zr-radiolabeled micelles samples on iTLC-SG using acetonitrile/citric acid (20 mm, adjusted at pH 4.9–5.1 with 2 M Na_2CO_3) 1 : 9 v/v as eluent.

A remarkable stability of the radiolabeling was observed for DiD@pDA–PEG/DFO[^{89}Zr] micelles incubated in serum for 48 h and at 37 °C (Fig. S4†). Radio-iTLC analyzes showed that ^{89}Zr remained complexed with micelles and no significant release was detected despite the presence of serum proteins and enzymes.

In vivo biodistribution study by bimodal PET/optical imaging and *ex vivo* gamma counting analyses

The distribution of micelles was evaluated on a group of mice bearing subcutaneous U-87 MG tumors either with (n = 6) or without (n = 6) US/μBs treatment. Thanks to DiD encapsulation and ^{89}Zr-labelling at the surface of the micelles, both optical and PET imaging techniques could be used simultaneously to evaluate the delivery and biodistribution of DiD@pDA–PEG/DFO[^{89}Zr] micelles. When the tumor reached a sufficient volume to be imaged (~200 mm^3), mice were injected with the DiD@pDA–PEG/DFO[^{89}Zr] micelles simultaneously with or without microbubbles coupled with ultrasound. Directly after the ultrasound protocol (2 min), mice were imaged under the PET camera during one hour (dynamic acquisition). Then, a static PET acquisition was performed 4 h, 24 h, 48 h, 72 h and 7 days after the injection. Whole-body images at the maximum concentration accumulation time, *i.e.* 48 h after micelle injection, are displayed in Fig. 2A and B. The whole dynamic kinetics at different time points is presented in Fig. S7 and S8.† Both imaging techniques allowed the visualization of the retention of DiD@pDA–PEG/DFO[^{89}Zr] micelles in the tumor area between 24 and 72 h post injection (p.i.). Micelles were also detected in the liver area, which is classically observed with nanometric carrier systems. These observations were confirmed by *ex vivo* fluorescence images of the organs obtained 7 days p.i. (Fig. S5†).

Thanks to the long half-life of ^{89}Zr, PET imaging allows longitudinal quantification of the micelles even after one week.[38] For the control group, the accumulation of DiD@pDA–PEG/DFO[^{89}Zr] micelles in the main organs was quantified with respect to activity deposited in tissues using volume-of-interest (VOI) analysis on PET images only (Fig. 2C). A relatively long blood-circulation of the DiD@pDA–PEG/DFO[^{89}Zr] micelles was observed. In fact, 17% of the activity was still present in the blood 24 h post-injection.

Concerning the elimination pathway, the early activity detected in the bladder, which almost totally vanished after 4 h p.i., suggests that a small fraction of the micelles was eliminated in the urine shortly after administration. However, the high radioactivity signal present in the liver and spleen, which increased up to 48 h followed by a slow decrease, clearly demonstrated that micelles were mainly excreted by the hepato-biliary system.

For the tumor uptake, the maximal accumulation in the tumor (*ca.* 3 %ID cm^{-3}) occurred 48 h after injection and slowly decreased to reach 2.3 %ID cm^{-3}, one-week p.i. Therefore, most of the DiD@pDA–PEG/DFO[^{89}Zr] micelles that reached the target were retained by the tumor. Minor retention in bones (known feature of ^{89}Zr-labeled compounds) and

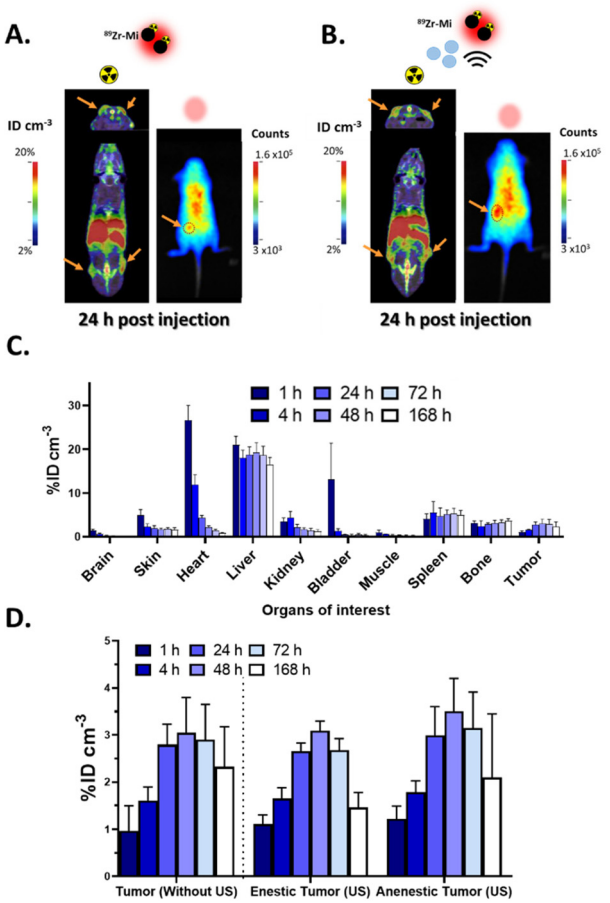

Fig. 2 *In vivo* biodistribution of DiD@pDA–PEG/DFO[^{89}Zr] micelles in subcutaneous U87-MG tumor model. PET (coronal-upper and axial-lower) and optical images obtained from mice (more information in Fig. S6 and S7†) (A) without or (B) with US, 24 h after injection of DiD@pDA–PEG/DFO[^{89}Zr] micelles (150 μL, 10 mg mL^{-1}, 113 μCi). The orange arrows indicate the position of the tumors, and the red dot circle shows the enestatic tumor. (C) Biodistribution derived from PET imaging of DiD@pDA–PEG/DFO[^{89}Zr] micelles over time into the main organs without US exposure (n = 6). (D) Quantitative DiD@pDA–PEG/DFO[^{89}Zr] micelles accumulated into the tumors without US, with US (enestic and anenestic tumors) (n = 6). Results are represented as %ID cm^{-3} mean ± standard deviation.

brown fat (common for lipidic nanoparticles) was also observed as further elaborated in the discussion part. As expected, almost no signal was detected in the brain or the muscle at any time point.

Finally, comparison of DiD@pDA–PEG/DFO[^{89}Zr] micelles accumulation with and without US in the tumors over time was determined by PET imaging analysis (Fig. 2D). The sonoporation protocol was established based on previous studies, considering the limited half-life of the microbubbles within the bloodstream.[39] Similar accumulation profiles were obtained for the tumor in contact with US transducer (enestic tumor: 3.1 %ID cm^{-3} at 48 h, and 1.5 %ID cm^{-3} after 1 week) and the contralateral tumor (anenestic tumor: 3.5 %ID cm^{-3} at 48 h, and 2.1 %ID cm^{-3} after 1 week). Nevertheless, it can be noticed that US/μBs exposure induced a more homogenous delivery of micelles into the enestic tumor as the standard deviation of micelles accumulation was significantly reduced compared to the anenestic tumor.

Pharmacokinetic study derived from PET imaging of DiD@pDA–PEG/DFO[^{89}Zr] micelles with and without US

Based on PET quantification, modeling blood kinetics was performed using the blood pool VOI (Fig. 3A). Exponential fitting revealed a biphasic elimination process from the circulation with a fast α-phase, and a longer β-phase for DiD@pDA–PEG/DFO[^{89}Zr] micelles without US treatment ($t_{\frac{1}{2}}\alpha$ = 136 ± 33 min; $t_{\frac{1}{2}}\beta$ = 40.6 ± 11.8 h) and with US/μBs ($t_{\frac{1}{2}}\alpha$ = 128 ± 39 min; $t_{\frac{1}{2}}\beta$ = 30.8 ± 5.9 h).

On the other hand, no significant difference was observed in the accumulation (AUC in %ID cm^{-3} h) of DiD@pDA–PEG/DFO[^{89}Zr] micelles in non-treated mice (475.5 ± 79.7) compared to mice treated with US/μBs in either the enestic (384.7 ± 20.39) or anenestic tumors (462.8 ± 76.8) (Fig. 3B). Again, the most striking effect was found to be the reduction of the standard deviation in the enestic tumor.

Ex vivo characterization of US impact on DiD@pDA–PEG/DFO [^{89}Zr] micelle delivery

Tumors were harvested 72 h or 1 week after injection, and post-mortem distribution of DiD@pDA–PEG/DFO[^{89}Zr]

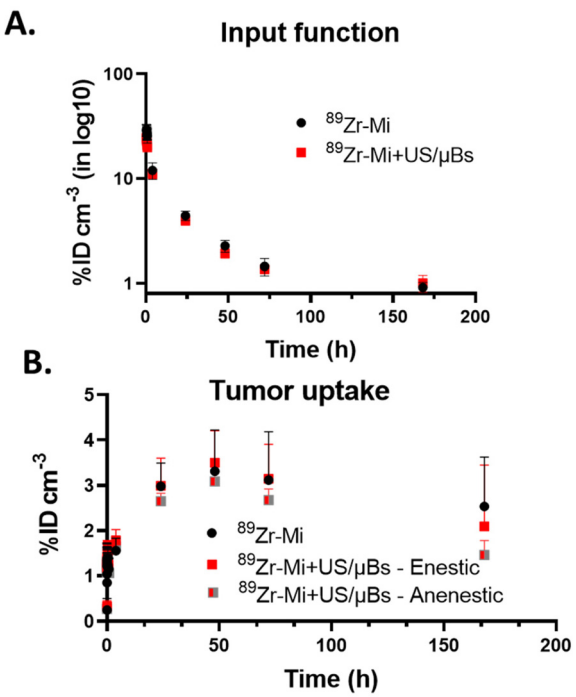

Fig. 3 *In vivo* kinetic of DiD@pDA–PEG/DFO[^{89}Zr] micelles: micelles without (black) or with US (red for the enestic tumor and grey/red for the anenestic tumor) exposure, in subcutaneous tumor model (n = 6) derived from PET images until one week. (A) The blood time activity curves (TAC) and (B) the tumors TACs (without US, with US for the enestic and anenestic tumors). Results are represented as %ID cm^{-3} mean ± standard deviation.

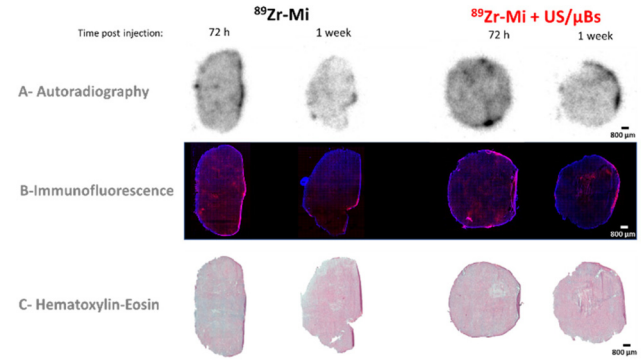

Fig. 4 Histological analyses of adjacent slices from tumors without (left) or with US (right) exposure, collected 72 h and one week after injection of DiD@pDA–PEG/DFO[^{89}Zr] micelles (150 μL, 10 mg mL^{-1}, 113 μCi). (A) Autoradiography (B) immunofluorescence and (C) hematoxylin–eosin staining. The scale bare: 800 μm.

micelles was assessed by autoradiography, fluorescence and histological analysis of tissue sections (Fig. 4). DiD@pDA–PEG/DFO[^{89}Zr] micelles were first visualized by autoradiography. The adjacent sections were observed by optical imaging (Fig. S6 and S7†). Tumor heterogeneity such as higher cellular density and the presence of few small necrotic areas were visualized on each slide by hematoxylin–eosin staining. Colocalization between autoradiography and fluorescence signals confirmed the effective delivery of DiD@pDA–PEG/DFO [^{89}Zr] micelles to the entire tumor tissue without significant differences between the periphery, the center, the necrotic and parts of the tumor with higher cell density. The few regions with higher signal on the border were due to folding of the slices. In agreement with the *in vivo* analyses, a small decrease of the signal was observed between 72 h and one week due to a slow washout. However, the fluorescence signal coming from the micelles was clearly visible even one week after injection (Fig. S8†), which confirmed strong *in vivo* stability. These results highlight the high diffusion potential of the DiD@pDA–PEG/DFO[^{89}Zr] micelles within the whole tumor volume, but no difference could be observed between the two groups (Fig. S8C†).

Discussion

In most preclinical studies, micelles are monitored using either fluorophores,[40,41] or radio-ligands.[42,43] However, the low penetration depth, poor spatial resolution, and poor quantification capabilities of optical imaging,[44] could lead to imprecise or even inexact localization of micelles and/or drugs. It is thus of prime importance to develop techniques that allow accurate localization of both the micelles and their payload. Classical micelles also suffer from dissociation upon dilution, for example in the blood flow.[9,45] We thus used in this study polymerizable amphiphiles to form stable polydiacetylene micelles that were loaded with a near-infrared fluorophore (in their core) and radiolabelled with ^{89}Zr (at their surface) though complexation with DFO ligands. ^{89}Zr could be tracked by PET imaging, a highly sensitive functional technique with suitable temporal resolution, quantification and penetration depth.[44,46] The radiolabeling step did not impact the fluorescence properties of the micelles, and physicochemical characterizations showed good radiochemical stability of DiD@pDA–PEG/DFO [^{89}Zr] micelles. Therefore, we successfully synthesized bimodal DiD@pDA–PEG/DFO[^{89}Zr] micelles that allow tracking by both PET and optical imaging.

The pharmacokinetics and biodistribution of the DiD@pDA–PEG/DFO[^{89}Zr] micelles were evaluated in mice bearing subcutaneous U87-MG tumors, using longitudinal optical and PET imaging. It is important to note that no toxicity has been observed with these micelles, which is consistent with the findings of previous studies involving equivalent micelles.[47] The micelles were well tolerated by the mice and displayed extended circulation in the bloodstream. Maximum accumulation in the tumor was observed 48 h post-injection.

Despite the advantage of optical imaging in terms of spatial resolution, PET imaging can assess the tissue distribution of the radiolabelled micelles over time. DiD@pDA–PEG/DFO [^{89}Zr] micelles showed predominant retention in the liver and the spleen, suggesting excretion by the hepatic system. These findings indicate the uptake of micelles by the mononuclear phagocytic system, as previously described by Perrault *et al.* (Fig. SI1.D†).[48] In addition, brown fat showed increased radioactivity as already reported for other lipidic nanoparticles.[49] Bone uptake reflects the release of ^{89}Zr due to a transmetalation phenomenon but this is considerably lower than that observed with [^{89}Zr]-chloride, -oxalate, -citrate or -DFO, suggesting improved stability of the radiolabeled micelles *in vivo*.[38,50–52]

DiD@pDA–PEG/DFO[^{89}Zr] micelles exhibited passive tumor accumulation that was maximal (3.1 ± 1.1 %ID cm^{-3}) at 48 h p.i., with high tumor-to-muscle ratio (8.6 ± 2.7). This passive uptake is mediated by the EPR effect, and the micelles were retained in the tumor up to 7 days with slow washout. *Ex vivo* autoradiography and fluorescence microscopy support PET-images analysis. Co-localization of the radioactive and fluorescent signals on tumor slides confirms the good *in vivo* stability of the NPs up to one week after injection. Furthermore, the micelles were found to be effective in delivering and distributing the drug mimic DID throughout the tumor volume, with no significant difference between the core and the periphery. Their small size likely helped reaching deeper tumor tissues, as reported in other studies using NPs of similar size.[53,54]

In order to increase the distribution of micelles in the whole tumor, we transiently enhanced the permeability of blood vessels using a non-invasive technique that combines US and microbubbles. In a previous study, we demonstrated that sonoporation associated to irinotecan significantly improved the reduction of the tumor volume compared to irinotecan treatment alone in subcutaneous glioblastoma bearing mice (U-87 MG).[55] Despite the use of similar US parameters, μBs and tumor model, here sonoporation did not sig-

nificantly improve the accumulation of DiD@pDA–PEG/DFO [^{89}Zr] micelles in the tumors (compared to the group without US). No statistically significant difference was found based on ANOVA analysis (α = 0.05). However, a significant decrease in the standard deviation of micelle accumulation was observed in the tumor directly in contact with the US source (compared to the tumor located on the opposite flank of the mouse). This observation suggests that US helps delivering DiD@pDA–PEG/DFO[^{89}Zr] micelles more homogenously into the tumor and might induce a beneficial therapeutic effect. Even though US induces a temporary disruption of the walls of blood vessels, preclinical studies on rodent have shown no short-time adverse effects.[56] Therefore, microbubble-assisted ultrasound might be a safe technique to achieve the homogeneous delivery of micelles to subcutaneous tumors. Further studies will be necessary to evaluate the therapeutic benefits of chemotherapy encapsulated in micelles assisted by sonoporation in more sophisticated tumor models particularly in orthotopic tumor models.

Experimental section

Materials

Citric acid monohydrate ($C_6H_6O_7$, $H_2O \geq 99\%$), phosphate buffered saline (PBS) tablets, buffer formalin 10%, were purchased from Sigma-Aldrich (France). Sodium carbonate (Na_2CO_3) was purchased from VWR (France). Zirconium-89 [^{89}Zr]Zr-oxalic acid was obtained from PerkinElmer (Netherlands). H_2O Optimal LC/MS and 2-methylbutan were purchased from Fisher chemical (Thermo Fisher Scientific, France) and Honeywell (France). Trifluroacetic acid, ethanol, acetonitrile were obtained from Carlo Erba (France). Isoflurane was purchased from Baxter (France). PD-10 desalting columns and instant thin–layer chromatography on glass microfiber chromatography paper impregnated with silica gel were purchased from GE Healthcare (France). Vivaspin® ultrafiltration tubes (5 kDa) were obtained from Sartorius (France). Prolong Diamond Antifade Mountain with DAPI was purchased from Invitrogen (Thermo Fisher Scientific, France) and optimum cutting temperature from Cell Path (United Kingdoms). Dulbecco's phosphate buffered saline (10 mm), Trypsin-EDTA, antibiotic–antimycotic, fetal bovine serum and cell culture medium (Dulbecco's Modified Eagle's medium) were purchased from Gibco (Thermo Fisher Scientific, France). Microbubbles (SonoVue®, 1.5×10^8 µB mL^{-1}) were purchased from Bracco (Milan, Italy). Ultrapure water (resistivity > 18 MΩ cm) was obtained using a Milli-Q system (Millipore, France) and used for all immunohistological buffers. All products were used as received without further purification. For organic synthesis, unless otherwise specified, all chemicals were purchased from Sigma-Aldrich and used without further purification. Flash chromatography was carried out on Kieselgel 60 (230–240 mesh, Merck). ^{1}H NMR spectra were recorded using a Bruker Avance DPX 400 spectrometer at 400 MHz. Chemical shifts (δ) are given in ppm relative to the NMR solvent residual peak. Electrospray mass spectra were performed on an ESI Quadripole autopurify from Waters (pump 2545, mass: ZQ2000) Mass Spectrometer. Dynamic light scattering (DLS) analyses were recorded using a Vasco-Flex analyzer (Cordouan, France) equipped with a 450 nm laser. Milli-Q water (18 MΩ cm) was used to prepare micelle solutions.

Preparation of DiD-loaded micelles labeled with ^{89}Zr

Synthesis of amphiphiles (Schemes S1 and S2†)

*Synthesis of pentacosa-10,12-diyn-1-ol (**1**).* To a solution of 10,12-pentacosadiynoic acid (1.0 g, 2.7 mmol, 1 equiv.) in anhydrous diethyl ether (44 mL), lithium aluminum hydride (0.2 g, 5.4 mmol, 2 equiv.) was added slowly, at 0 °C under nitrogen. The mixture was stirred at room temperature for 1.5 h. The reaction was monitored by TLC using cyclohexane/ethyl acetate (1 : 1 v/v). The mixture was cooled to 0 °C and water (200 µL) was added, followed by 15 wt% NaOH (200 µL), and more water (600 µL). The mixture was then filtered on Celite and the residue was washed with diethyl ether several times. The organic phase was washed with 1 M HCl (20 mL). The organic layer was collected, dried over $MgSO_4$, filtered and concentrated under vacuum to afford **1** (783 mg, 81%) as a white solid.

^{1}H NMR (400 MHz, $CDCl_3$): δ 3.63 (t, J = 6.9 Hz, 2H), 2.23 (t, J = 6.9 Hz, 4H), 1.62–1.44 (m, 7H), 1.43–1.18 (m, 28H), 0.87 ppm (t, J = 6.9 Hz, 3H).

*Synthesis of 1-bromopentacosa-10,12-diyne (**2**).* To a solution of **1** (0.43 g, 1.2 mmol, 1 equiv.) and triphenylphosphine (0.47 g, 1.8 mmol, 1.5 equiv.) in anhydrous CH_2Cl_2 (3 mL), carbon tetrabromide (0.59 g, 1.8 mmol, 1.5 equiv.) was added under nitrogen. The brown mixture was stirred for 1 h, then cold water (10 mL) was added. The organic phase was washed with water (3 × 20 mL). The combined organic layers were dried over $MgSO_4$, filtered and concentrated under vacuum. The brown crude product was purified on silica gel using 100% CH_2Cl_2 to afford **2** (300 mg, 59%) as a yellowish waxy solid.

^{1}H NMR (400 MHz, $CDCl_3$): δ 3.39 (t, J = 6.9 Hz, 2H), 2.23 (t, J = 6.9 Hz, 4H), 1.89–1.78 (m, 2H), 1.56–1.45 (m, 4H), 1.45–1.17 (m, 28H), 0.87 ppm (t, J = 6.9 Hz, 3H).

*Synthesis of **DA–PEG**.* Under nitrogen atmosphere, to a stirred suspension of sodium hydride (94 mg (60% in oil), 1.98 mmol, 2.2 equiv.) in dry THF (8 mL) was added a solution of methoxypoly(ethylene glycol) 2000 (MW = 2 000, 2 g, 1 mmol, 1.1 equiv.) in dry THF (10 mL). The reaction mixture was protected from light and was stirred for 30 min at 85 °C. A solution of **2** (380 mg, 0.9 mmol, 1.0 equiv.) in dry THF (3 mL) was added at room temperature to the above mixture. After 3 days at room temperature and under nitrogen atmosphere, the reaction was quenched with the addition of water (200 µL). The mixture was then filtered, dried over anhydrous $MgSO_4$, filtered again, and the solvent was evaporated under vacuum. The crude product was purified by column chromatography (silica gel, CH_2Cl_2/MeOH 96 : 4) and pure **DA–PEG** was obtained as a pale beige solid (1 g, 40%).

^{1}H NMR (400 MHz, $CDCl_3$): δ 3.78–3.33 (m, 212H), 3.31 (s, 3H), 2.17 (t, J = 7.0 Hz, 4H), 1.54–1.37 (m, 6H), 1.35–1.10 (m, 32H), 0.81 ppm (t, J = 6.8 Hz, 3H).

*Synthesis of 2,5-dioxopyrrolidin-1-yl pentacosa-10,12-diynoate (**3**).* A solution of 10,12-pentacosadiynoic acid (1.00 g, 2.7 mmol, 1 equiv.), *N*-hydroxysuccinimide (0.35 g, 3.0 mmol, 1.1 equiv.), 1-ethyl-3-(3-dimethylaminopropyl)carbodiimide hydrochloride (0.60 g, 3.2 mmol, 1.2 equiv.) in anhydrous CH_2Cl_2 (25 mL) was stirred for 14 h at room temperature under nitrogen. Water (20 mL) was added to the mixture. The aqueous phase was extracted with CH_2Cl_2 (3 × 20 mL). The combined organic layers were dried over $MgSO_4$, filtered and concentrated under vacuum to afford **3** (1.14 g, 90%) as a white solid.

^{1}H NMR (400 MHz, $CDCl_3$): δ 2.89–2.79 (m, 4H), 2.60 (t, J = 7.5 Hz, 2H), 2.24 (t, J = 6.9 Hz, 4H), 1.74 (dt, J = 15.2 Hz, 7.5 Hz, 2H), 1.55–1.45 (m, 4H), 1.44–1.20 (m, 26H), 0.88 ppm (t, J = 6.9 Hz, 3H).

*Synthesis of **DA–DFO**.* To a solution of deferoxamine mesylate salt (0.131 g, 0.20 mmol, 1.0 equiv.) in phosphate-buffered saline 0.1 M (4 mL, pH = 7.4) was added a solution of **3** (0.100 g, 0.24 mmol, 1.2 equiv.) in tetrahydrofuran (4 mL). The mixture was stirred at room temperature under nitrogen for 48 h. The mixture was concentrated under vacuum until dryness. Water (30 mL) was then added to the crude product and the flask was placed in an ice bath. The suspension was then filtered and successively washed with cold water (60 mL), cold saturated sodium carbonate solution (60 mL), cold water (60 mL), cold acetone (20 mL) and cold diethyl ether (60 mL) to afford **DA–DFO** (106 mg, 51%) as a white solid.

ESI-MS calculated for $C_{50}H_{89}N_6O_9$ $[M + H]^+$ 917.7, found 917.3.

Micelle preparation

Micelle assembly and polymerization. **DA–PEG** (45 mg) and **DA–DFO** (5 mg) were dispersed in water (5 mL) and the mixture was sonicated with an ultrasonic probe (300 ms pulse per second, output 45%, Branson 550 Sonifier) for 10 min, affording a clear micellar colloid. The mixture was transferred to a crystallizing dish and photopolymerized under UV irradiation (254 nm, low pressure mercury UV lamp, 40 W from Heraeus) for 3 h, yielding pDA–PEG/DFO micelles. The colloid was then filtered on a 0.22 μm membrane and characterized by DLS at 25 °C. Measurements were recorded over 6 consecutive runs of 60 s each.

Dye encapsulation. DiD (1,1′-dioctadecyl-3,3,3′,3′-tetramethylindodicarbocyanine, 4-chlorobenzenesulfonate Salt, 0.1 mg) dissolved in chloroform (0.1 mL) was added to pDA–PEG/DFO colloid (1 mL). The biphasic mixture was sonicated with an ultrasonic probe (300 ms pulse per second, output 45%, Branson 550 Sonifier) for 10 min and then allowed to cool down to room temperature over 10 min. The process was repeated two more times for a total of 3 sonication cycles after which a blue colloid of DiD@pDA–PEG/DFO was obtained. The latter was filtered on a 0.22 μm membrane to remove any free dye from the suspension. The amount of dye encapsulated in the micelles was confirmed (0.8 wt%) by UV-vis spectroscopy. DiD@pDA–PEG/DFO micelles were finally purified through a PD-10 column using H_2O Optimal LC/MS as mobile phase and their fluorescence spectrum was recorded on a CLARIOstar Plus spectrophotometer (BMG LABTECH) between 606 and 795 nm (λ_{exc} = 575 nm). The micelles were freeze-dried and stored at 4 °C until radiolabeling.

Micelle radiolabeling with zirconium-89. On the day of imaging experiments, a suspension of DiD@pDA–PEG/DFO micelles (8.96 mg, 3 mg mL^{-1} in H_2O Optimal LC/MS) was adjusted at pH 7.2 by adding 0.01 M HCl (5 μL). The oxalic acid of the ^{89}Zr solution (320 μL, 237 MBq) was neutralized with 2 M Na_2CO_3 (192 μL) before addition to the DiD@pDA–PEG/DFO suspension. The mixture was stirred for 1 h at 50 °C and 500 rpm to complete the reaction. DiD@pDA–PEG/DFO [^{89}Zr] was purified through PD-10 column using phosphate buffered saline (PBS) as mobile phase and concentrated by Vivaspin® ultrafiltration tubes (5 kDa cutoff).

Stability of DiD@pDA–PEG/DFO[^{89}Zr] micelles in mouse plasma and serum. The stability study was designed so that the ratio between the volume of serum (or plasma) and the volume of DiD@pDA–PEG/DFO[^{89}Zr] micelles was higher than the theoretical 0.25 : 0.075 ratio of *in vivo* experiments (described below). For each 30 μL of radiolabeled micelles (1 mg, 17 MBq), 120 μL of either PBS, mouse plasma or mouse serum was added. Samples were analyzed by thin–layer chromatography (TLC) right after mixing (0 h), after 24 h and 48 h of incubation at 37 °C and 500 rpm.

Characterization of DiD@pDA–PEG/DFO[^{89}Zr] micelles. The radiochemical yield and purity were determined using instant thin–layer chromatography on glass microfiber chromatography paper impregnated with silica gel (iTLC-SG) as stationary phase and citric acid solution (20 mM, pH adjusted to 4.9–5.1 with 2 M Na_2CO_3) with 10% of acetonitrile as mobile phase. The elution was followed by radio–TLC detection (Mini-Scan TLC Imaging Scanner, Eckert & Ziegler, Berlin, Germany) and by exposition to a storage phosphor screen (VWR) in an exposure cassette (Molecular Dynamics) for 20 min at room temperature (RT) before developing the screen with Storm 860 Molecular Imager (50 μm resolution).

High performance liquid chromatography (HPLC) allowed measuring the complexation of [^{89}Zr] by the DA–DFO and therefore determining the radiopurity of the final DiD@pDA–PEG/DFO radiolabeled micelles. HPLC was performed on a Dionex system (ThermoFisher Scientific, France) with a P680HPLC pump, an oven column compartment (TCC-100 at 30 °C), a UV-vis (UVD170U UV/VIS) and a scintillation detector (Packard, Canberra, Austria) detector. A reversible phases Jupiter C4 column (150 mm × 4.60 mm, 5 μm, 300 Å, 16 496 Phenomenex) was used to separate the different diacetylene amphiphiles (PEG and DFO) according to an established protocol.[14] Briefly, 20 μL of sample at 20 μCi was injected into the column and a linear-gradient elution was carried out with a solution of (A) Milli-Q water/trifluroacetic acid (TFA) 99.9 : 0.1 v/v and (B) acetonitrile (MeCN)/TFA 99.9 : 0.1 v/v, at a flow rate of 1 mL min^{-1}. The elution was programmed as: 1% of solvent B during 5 min to elute the reactive, then a gradient from 1%

to 90% in 13 min followed by 90% of solvent B during 4 min to elute the fragment and the micelles and finally 1% of B during 7 min to wash the column. Eluted species were detected *via* UV and radioactivity detection.

Cell culture

Human U-87 MG cells derived from human astrocyte glioblastoma grade III, were purchased from ATCC (HTB-14). Cells were cultured in a humidified incubator (Sanyo, Japan) at 37 °C in an atmosphere containing 5% of CO_2 in DMEM (Dulbecco's Modified Eagle's medium) supplemented with 10% of heat-inactivated FBS (fetal bovine serum), 1% antibiotic–antimycotic (streptomycine, amphotericin B, penicillin). Mycoplasma absence was confirmed using MycoAlert™ kit (Lonza, USA).

Animal experiments

Animal experiments were conducted in agreement with the European Directive 2010/63/EU on the protection of laboratory animals (French law transposition: decree no. 2013-118). They were performed at the imaging facility CEA-SHFJ with protocols approved by the Ethical Committee of CETEA-CEA DSV IdF (authorization D91-471-105). In total, 16 five-week-old female athymic NMRI nude mice were purchased from Janvier laboratories (Le Genet sur Isle, France, Mus musculus, NMRI-FOXN1 Nu/Nu). Mice were housed, four per cage, with food and water *ad libitum* in an enriched environment (polycarbonate cottages and wooden stocks), in a room with controlled temperature (22 °C) and humidity (40%), and were maintained under specific pathogen-free conditions.

Sub-cutaneous tumor model

Mice anesthetized with isoflurane (4% in O_2 for induction and 2% in O_2 for maintenance) received a subcutaneous injection of 5.0×10^6 U87 cells suspended in 100 μL of PBS in both right and left flanks for heterotopic establishment of tumors. Animal weight and tumor growth were monitored three times a week. The tumors were allowed to grow for three weeks before the beginning of the experiments. At the end of the experiments, mice were euthanized by cervical dislocation under isoflurane (5%). Tumors were removed, immersed in 2-methylbutan and frozen in liquid nitrogen.

Sonoporation using US

US procedure. Animal experiments were performed under Isoflurane anesthesia (4% for induction and 2% for maintenance) in a mixture of air/O_2 8 : 2. The US procedure was similar to the protocol in our previous study.[55]

Briefly, US were delivered using a transducer (active diameter 5 mm, focal depth 3 cm, Imasonic, Voray sur l'Ognon, France) connected to a programmable generator (Image Guided Therapy, Pessac, France). The transducer was mounted on a 3D-printed custom holder to ensure a 3 cm distance between the tumor and the transducer. An acoustic window (TPX membrane) was made at the front of the holder and the transducer was immersed into with deionized and degassed water. Acoustic gel was added between the holder and the animal skin to ensure ultrasound transmission. A 50 μL bolus of SonoVue® was intravenously administered in the tail vein. The US opening covered a circular region centered on the subcutaneous tumor (5 mm in diameter) and allowed deep penetration (up to 2 cm) (Fig. S9†). Ultrasonic waves were transmitted at 1.0 MHz during 2 min with a duty cycle of 40% and a pulse repetition frequency of 10 kHz. The transmitted *in situ* peak negative pressure in the tumor was estimated to be 400 kPa.

Sonoporation protocol was performed on mice bearing U-87 MG subcutaneous tumors. Each mouse carried two tumors, one in each flank. The US procedure was applied in only one tumor flank (the enestic tumor). Due to the deep penetration of the US, the tumor present on the other flank within the same mouse (the anenestic tumor) could be open at a lower degree. A group of mice that did not received US waves was used as a negative control (without US).

PET acquisition and image reconstruction

PET acquisitions were performed using the Inveon microPET-CT (Siemens Medical Solutions, Knoxville, TN, USA). The spatial resolution of the PET scanner is ~1.5 mm (FWHM). After the PET scan, a 6 min 80 kV per 500 μA CT scan was performed for attenuation correction. PET images were reconstructed using a 3D OSEM iterative algorithm (4 iterations, 16 subsets, voxel size = 0.4 mm × 0.4 mm × 0.8 mm). Normalization, dead time correction, random subtraction, CT-based attenuation and scatter corrections were applied.

Longitudinal PET evaluation of DiD@pDA–PEG/DFO[^{89}Zr] micelle tumor accumulation with and without US

Imaging protocol. Three weeks after tumor implantation, a total of 12 mice were randomized into 2 groups that received intravenous injection of μB (Sonovue, 50 μL) and DiD@pDA–PEG/DFO[^{89}Zr] micelles (150 μL, 10 mg mL^{-1}, 4.18 ± 0.21 μCi) with or without US (n = 6 for each group). Dynamic PET scans of 60 min performed under the camera (framing: 3 × 30 s, 5 × 60 s; 5 × 120 s, 3 × 180 s, 3 × 240 s, 4 × 300 s, 1 × 240 s) were acquired immediately after injection of DiD@pDA–PEG/DFO [^{89}Zr] micelles into the tail vein. Then, a 20 min PET acquisition was performed 4 h, 24 h, 48 h, 72 h and 7 days after the injection. For one mouse per group, optical imaging was acquired prior to injection, 24 h, 48 h, 72 h and 7 days after the injection. One mouse per group was sacrificed by cervical dislocation under isoflurane (5%) 72 h post-injection. The tumor directly in contact with the transducer was removed, immersed in 2-methylbutan, frozen in liquid nitrogen and stored at −80 °C until histological analysis (auto-radiography, immunofluorescence, and hematoxylin–eosin staining). The timeline of the experiments is shown in Fig. S10.†

Image analysis. Imaging analyses were performed with the PMOD software (Version 3.9, Switzerland). All images and extracted data were corrected according to the half-life of ^{89}Zr ($t_{\frac{1}{2}}$ = 3.3 days).

The accumulation of DiD@pDA–PEG/DFO[^{89}Zr] micelles in the different organs of interest (brain, skin, heart, liver, kidneys, bladder, muscle, spleen and bone) were measured by positioning a VOI of 8.0 mm^3 in the middle of the organ.

The accumulation of DiD@pDA–PEG/DFO[^{89}Zr] micelles in the tumor was measured by drawing the iso-contour of the tumor at 48 h, which corresponds to the maximal tumor accumulation time. Then the same VOI was used for other time points.

The activities were expressed using the following formula:

$$\%\mathrm{ID\,cm^{-3}} = \frac{\mathrm{activity(kBq)}\ \textit{per}\ \mathrm{cm^3\ of\ tissue}}{\mathrm{injected\ activity(kBq)}} \times 100$$

After the last acquisition, mice were sacrificed by cervical dislocation under isoflurane (5%). The tumor directly in contact with the transducer was removed, immersed in 2-methylbutan and frozen in liquid nitrogen. The main organs (brain, heart, liver, left kidney, the tumor that was not directly in contact with the transducer, muscle, spleen, and bone) were collected and weighed. The radioactivity in these tissues was counted in a gamma counter (Cobra II 576 autogamma, Packard). Tissue uptake was expressed as % of injected activity per g of tissue.

The correlation between the DiD@pDA–PEG/DFO[^{89}Zr] micelle accumulation value determined from images and gamma counter was assessed through Pearson's correlation coefficient.

Blood pharmacokinetics. Blood activity concentrations were determined from the blood pool activity issued from PET image VOI. The radioligand blood half-life contributions were interpolated with a tri-exponentials model from blood time-activity curves from each individual mouse using the PMOD kinetic modeling tool (v4.2). The areas under the curve (AUC) were compared between the group without US and the group with US.

Histological analysis

Tissue section process. Serial tumor sections (14 μm thick) were cut at −20 °C with a cryostat (Leica CM3050 S, Leica biosystems) and adhered on SuperFrost Ultra Plus TM slides (FisherScientific). Slides were stored at −80 °C until histological analysis (hematoxylin–eosin, autoradiography, and immunofluorescence).

Autoradiography. Tumor slides were exposed to a storage phosphor screen (VWR) in an exposure cassette (Molecular Dynamics) for 24 h at 4 °C. The screen was developed with Storm 860 Molecular Imager at 50 μm resolution. Images were analyzed using ImageJ software (v1.53i).

Immunofluorescence staining. Frozen tumor slides were fixed in neutral buffer formalin 10% for 15 min at RT, then washed three times with PBS buffer. Slides were mounted using Prolong Diamond Antifade Mountain with DAPI. Fluorescence microscopy was performed on Axio Observer 5 microscope (Zeiss, Germany) at 20× and 40× magnifications. Image post-processing was performed with the ZEN software (v2.6, Zeiss).

Hematoxylin–eosin staining. Tumor slides were fixed in neutral buffer formalin 10% for 30 min then washed with distilled water. Standard hematoxylin and eosin (H&E) staining was performed using Harris hematoxylin and Eosin Y alcoholic (Sigma-Aldrich). Transmitted light images of stained tumor sections were acquired with the Axio Observer 5 microscope (Zeiss, Germany) at 20× magnification. Image post-processing was performed with the ZEN software (v2.6, Zeiss).

Statistical analysis

All data are presented as mean ± standard deviation. Statistical analyses were performed using GraphPad Prism software (Graph Pad software Inc., San Diego, USA). Comparisons of uptakes in different organs of interest issued from PET data with US and without US over time were performed *via* Mann Whitney *U* rank test. Statistical changes at the 95% confidence level ($P < 0.05$) were qualified as significant.

Conclusions

A new family of bimodal micelles for optical and PET imaging was developed and investigated *in vivo* in a subcutaneous glioblastoma (U-87 MG) mouse model. DiD@pDA–PEG/DFO[^{89}Zr] micelles showed interesting features: a safe behavior after intravenous injection with adequate tumor accumulation and good contrast enhancement of near infrared fluorescence and PET measurements that allowed monitoring of the biodistribution of micelles and their cargo. In addition, the present work demonstrates that sonoporation treatment might be a safe strategy to homogenize micelle delivery into the tumor. The next step will be to use micelles loaded with conventional chemo-pharmaceuticals to confirm the benefits of sonoporation in terms of therapeutic efficacy.

Author contributions

E. P. and S. H. conducted, performed and analysed the data. E. P., E. D., A. N., E. G. & C. T. wrote the manuscript. C. D., A. N., & M. H. supported and implemented methodology and performed data analysis. E. G. and C. T. conceived the study and supervised the project. All authors have given approval to the final version of the manuscript.

Conflicts of interest

There are no conflicts to declare.

Acknowledgements

This research work received partial financial support from the project ZIRMITEP, funded by the CEA – PTC Bottom up program. Estelle Porret was supported by the "Fondation pour

la Recherche Médicale" (FRM). This work is supported by a public grant overseen by the French National research Agency (ANR) as part of the Investissements d'Avenir D program, through the "ADI 2020" project funded by the IDEX Paris-Saclay, ANR-11-IDEX-0003-02.

References

1 A. Allegra, G. Penna, A. Alonci, V. Rizzo, S. Russo and C. Musolino, Nanoparticles in Oncology: The New Theragnostic Molecules, *Anti-Cancer Agents Med. Chem.*, 2011, **11**(7), 669–686, DOI: **10.2174/187152011796817682**.

2 M. Narvekar, H. Y. Xue, J. Y. Eoh and H. L. Wong, Nanocarrier for Poorly Water-Soluble Anticancer Drugs—Barriers of Translation and Solutions, *AAPS PharmSciTech*, 2014, **15**(4), 822–833, DOI: **10.1208/s12249-014-0107-x**.

3 A. A. Halwani, Development of Pharmaceutical Nanomedicines: From the Bench to the Market, *Pharmaceutics*, 2022, **14**(1), 106, DOI: **10.3390/pharmaceutics14010106**.

4 T. Lammers, S. Aime, W. E. Hennink, G. Storm and F. Kiessling, Theranostic Nanomedicine, *Acc. Chem. Res.*, 2011, **44**(10), 1029–1038, DOI: **10.1021/ar200019c**.

5 J. Gong, M. Chen, Y. Zheng, S. Wang and Y. Wang, Polymeric Micelles Drug Delivery System in Oncology, *J. Controlled Release*, 2012, **159**(3), 312–323, DOI: **10.1016/j.jconrel.2011.12.012**.

6 N. Majumder, N. G. Das and S. K. Das, Polymeric Micelles for Anticancer Drug Delivery, *Ther. Delivery*, 2020, **11**(10), 613–635, DOI: **10.4155/tde-2020-0008**.

7 B. Du, M. Yu and J. Zheng, Transport and Interactions of Nanoparticles in the Kidneys, *Nat. Rev. Mater.*, 2018, **3**(10), 358–374, DOI: **10.1038/s41578-018-0038-3**.

8 E. Blanco, H. Shen and M. Ferrari, Principles of Nanoparticle Design for Overcoming Biological Barriers to Drug Delivery, *Nat. Biotechnol.*, 2015, **33**(9), 941–951, DOI: **10.1038/nbt.3330**.

9 A. S. Mikhail and C. Allen, Block Copolymer Micelles for Delivery of Cancer Therapy: Transport at the Whole Body, Tissue and Cellular Levels, *J. Controlled Release*, 2009, **138**(3), 214–223, DOI: **10.1016/j.jconrel.2009.04.010**.

10 N. Mackiewicz, E. Gravel, A. Garofalakis, J. Ogier, J. John, D. M. Dupont, K. Gombert, B. Tavitian, E. Doris and F. Ducongé, Tumor-Targeted Polydiacetylene Micelles for In Vivo Imaging and Drug Delivery, *Small*, 2011, **7**(19), 2786–2792, DOI: **10.1002/smll.201100212**.

11 P. Zhang, F. Sun, S. Liu and S. Jiang, Anti-PEG Antibodies in the Clinic: Current Issues and beyond PEGylation, *J. Controlled Release*, 2016, **244**(Pt B), 184–193, DOI: **10.1016/j.jconrel.2016.06.040**.

12 J. Fang, H. Nakamura and H. Maeda, The EPR Effect: Unique Features of Tumor Blood Vessels for Drug Delivery, Factors Involved, and Limitations and Augmentation of the Effect, *Adv. Drug Delivery Rev.*, 2011, **63**(3), 136–151, DOI: **10.1016/j.addr.2010.04.009**.

13 D. Rosenblum, N. Joshi, W. Tao, J. M. Karp and D. Peer, Progress and Challenges towards Targeted Delivery of Cancer Therapeutics, *Nat. Commun.*, 2018, **9**(1), 1410, DOI: **10.1038/s41467-018-03705-y**.

14 J. M. Caster, A. N. Patel, T. Zhang and A. Wang, Investigational Nanomedicines in 2016: A Review of Nanotherapeutics Currently Undergoing Clinical Trials, *Wiley Interdiscip. Rev.: Nanomed. Nanobiotechnol.*, 2017, **9**(1), DOI: **10.1002/wnan.1416**.

15 V. Tran, F. Lux, N. Tournier, B. Jego, X. Maître, M. Anisorac, C. Comtat, S. Jan, K. Selmeczi, M. J. Evans, O. Tillement, B. Kuhnast and C. Truillet, Quantitative Tissue Pharmacokinetics and EPR Effect of AGuIX Nanoparticles: A Multimodal Imaging Study in an Orthotopic Glioblastoma Rat Model and Healthy Macaque, *Adv. Healthcare Mater.*, 2021, **10**(16), 2100656, DOI: **10.1002/adhm.202100656**.

16 H. Lee, A. F. Shields, B. A. Siegel, K. Miller, I. Krop, C. Ma, P. M. LoRusso, P. Munster, K. Campbell, D. F. Gaddy, S. C. Leonard, E. Geretti, S. Blocker, D. Kirpotin, V. Moyo, T. Wickham and B. S. Hendriks, 64Cu-MM-302 Positron Emission Tomography Quantifies Variability of Enhanced Permeability and Retention of Nanoparticles in Relation to Treatment Response in Patients with Metastatic Breast Cancer, *Clin. Cancer Res.*, 2017, **23**(15), 4190–4202, DOI: **10.1158/1078-0432.CCR-16-3193**.

17 A. Delalande, S. Kotopoulis, M. Postema, P. Midoux and C. Pichon, Sonoporation: Mechanistic Insights and Ongoing Challenges for Gene Transfer, *Gene*, 2013, **525**(2), 191–199, DOI: **10.1016/j.gene.2013.03.095**.

18 H.-L. Liu, C.-H. Fan, C.-Y. Ting and C.-K. Yeh, Combining Microbubbles and Ultrasound for Drug Delivery to Brain Tumors: Current Progress and Overview, *Theranostics*, 2014, **4**(4), 432–444, DOI: **10.7150/thno.8074**.

19 S. Hernot and A. L. Klibanov, Microbubbles in Ultrasound-Triggered Drug and Gene Delivery, *Adv. Drug Delivery Rev.*, 2008, **60**(10), 1153–1166, DOI: **10.1016/j.addr.2008.03.005**.

20 Z. Fan, R. E. Kumon and C. X. Deng, Mechanisms of Microbubble-Facilitated Sonoporation for Drug and Gene Delivery, *Ther. Delivery*, 2014, **5**(4), 467–486, DOI: **10.4155/tde.14.10**.

21 C.-Y. Lin, J.-R. Li, H.-C. Tseng, M.-F. Wu and W.-L. Lin, Enhancement of Focused Ultrasound with Microbubbles on the Treatments of Anticancer Nanodrug in Mouse Tumors, *Nanomedicine*, 2012, **8**(6), 900–907, DOI: **10.1016/j.nano.2011.10.005**.

22 Z. Kovacs, B. Werner, A. Rassi, J. O. Sass, E. Martin-Fiori and M. Bernasconi, Prolonged Survival upon Ultrasound-Enhanced Doxorubicin Delivery in Two Syngenic Glioblastoma Mouse Models, *J. Controlled Release*, 2014, **187**, 74–82, DOI: **10.1016/j.jconrel.2014.05.033**.

23 M. Aryal, N. Vykhodtseva, Y.-Z. Zhang, J. Park and N. McDannold, Multiple Treatments with Liposomal Doxorubicin and Ultrasound-Induced Disruption of Blood–Tumor and Blood–Brain Barriers Improve Outcomes in a Rat Glioma Model, *J. Controlled Release*, 2013, **169**(1–2), 103–111, DOI: **10.1016/j.jconrel.2013.04.007**.

24 J.-M. Escoffre, A. Novell, S. Serrière, T. Lecomte and A. Bouakaz, Irinotecan Delivery by Microbubble-Assisted Ultrasound: *In Vitro* Validation and a Pilot Preclinical Study, *Mol. Pharmaceutics*, 2013, **10**(7), 2667–2675, DOI: **10.1021/mp400081b**.

25 J. Ogier, T. Arnauld, G. Carrot, A. Lhumeau, J.-M. Delbos, C. Boursier, O. Loreau, F. Lefoulon and E. Doris, Enhanced Drug Loading in Polymerized Micellar Cargo, *Org. Biomol. Chem.*, 2010, **8**(17), 3902, DOI: **10.1039/c004134c**.

26 P. Neuberg, A. Perino, E. Morin-Picardat, N. Anton, Z. Darwich, D. Weltin, Y. Mely, A. S. Klymchenko, J.-S. Remy and A. Wagner, Photopolymerized Micelles of Diacetylene Amphiphile: Physical Characterization and Cell Delivery Properties, *Chem. Commun.*, 2015, **51**(58), 11595–11598, DOI: **10.1039/C5CC03820K**.

27 E. Gravel, B. Thézé, I. Jacques, P. Anilkumar, K. Gombert, F. Ducongé and E. Doris, Cellular Uptake and Trafficking of Polydiacetylene Micelles, *Nanoscale*, 2013, **5**(5), 1955, DOI: **10.1039/c2nr34149b**.

28 A. Doerflinger, N. N. Quang, E. Gravel, G. Pinna, M. Vandamme, F. Ducongé and E. Doris, Biotin-Functionalized Targeted Polydiacetylene Micelles, *Chem. Commun.*, 2018, **54**(29), 3613–3616, DOI: **10.1039/C8CC00553B**.

29 E. Gravel, J. Ogier, T. Arnauld, N. Mackiewicz, F. Ducongé and E. Doris, Drug Delivery and Imaging with Polydiacetylene Micelles, *Chem. – Eur. J.*, 2012, **18**(2), 400–408, DOI: **10.1002/chem.201102769**.

30 J.-L. Li, R. C. A. Sainson, C. E. Oon, H. Turley, R. Leek, H. Sheldon, E. Bridges, W. Shi, C. Snell, E. T. Bowden, H. Wu, P. S. Chowdhury, A. J. Russell, C. P. Montgomery, R. Poulsom and A. L. Harris, DLL4-Notch Signaling Mediates Tumor Resistance to Anti-VEGF Therapy In Vivo, *Cancer Res.*, 2011, **71**(18), 6073–6083, DOI: **10.1158/0008-5472.CAN-11-1704**.

31 S.-D. Li and L. Huang, Stealth Nanoparticles: High Density but Sheddable PEG Is a Key for Tumor Targeting, *J. Controlled Release*, 2010, **145**(3), 178–181, DOI: **10.1016/j.jconrel.2010.03.016**.

32 D. N. Pandya, N. Bhatt, H. Yuan, C. S. Day, B. M. Ehrmann, M. Wright, U. Bierbach and T. J. Wadas, Zirconium Tetraazamacrocycle Complexes Display Extraordinary Stability and Provide a New Strategy for Zirconium-89-Based Radiopharmaceutical Development, *Chem. Sci.*, 2017, **8**(3), 2309–2314, DOI: **10.1039/C6SC04128K**.

33 C. Truillet, F. Lux, O. Tillement, P. Dugourd and R. Antoine, Coupling of HPLC with Electrospray Ionization Mass Spectrometry for Studying the Aging of Ultrasmall Multifunctional Gadolinium-Based Silica Nanoparticles, *Anal. Chem.*, 2013, **85**(21), 10440–10447, DOI: **10.1021/ac402429p**.

34 **https://Biotium.Com/Product/Did-Diic185-or-11-Dioctadecyl-3333-Tetramethylindodicarbocyanine-4-Chlorobenzenesulfonate-Salt/**.

35 **https://www.Interchim.Fr/Ft/4/46804A.Pdf**.

36 F. Guérard, Y.-S. Lee, R. Tripier, L. P. Szajek, J. R. Deschamps and M. W. Brechbiel, Investigation of Zr (IV) and ^{89}Zr(IV) Complexation with Hydroxamates: Progress towards Designing a Better Chelator than Desferrioxamine B for Immuno-PET Imaging, *Chem. Commun.*, 2013, **49**(10), 1002–1004, DOI: **10.1039/C2CC37549D**.

37 C. Truillet, E. Thomas, F. Lux, L. T. Huynh, O. Tillement and M. J. Evans, Synthesis and Characterization of 89Zr-Labeled Ultrasmall Nanoparticles, *Mol. Pharmaceutics*, 2016, **13**(7), 2596–2601, DOI: **10.1021/acs.molpharmaceut.6b00264**.

38 S. Heskamp, R. Raavé, O. Boerman, M. Rijpkema, V. Goncalves and F. Denat, ^{89}Zr-Immuno-Positron Emission Tomography in Oncology: State-of-the-Art ^{89}Zr Radiochemistry, *Bioconjugate Chem.*, 2017, **28**(9), 2211–2223, DOI: **10.1021/acs.bioconjchem.7b00325**.

39 K. Kooiman, S. Roovers, S. A. G. Langeveld, R. T. Kleven, H. Dewitte, M. A. O'Reilly, J.-M. Escoffre, A. Bouakaz, M. D. Verweij, K. Hynynen, I. Lentacker, E. Stride and C. K. Holland, Ultrasound-Responsive Cavitation Nuclei for Therapy and Drug Delivery, *Ultrasound Med. Biol.*, 2020, **46**(6), 1296–1325, DOI: **10.1016/j.ultrasmedbio.2020.01.002**.

40 B.-X. Zhao, Y. Zhao, Y. Huang, L.-M. Luo, P. Song, X. Wang, S. Chen, K.-F. Yu, X. Zhang and Q. Zhang, The Efficiency of Tumor-Specific PH-Responsive Peptide-Modified Polymeric Micelles Containing Paclitaxel, *Biomaterials*, 2012, **33**(8), 2508–2520, DOI: **10.1016/j.biomaterials.2011.11.078**.

41 Y. Chen, W. Zhang, Y. Huang, F. Gao and X. Fang, In Vivo Biodistribution and Anti-Tumor Efficacy Evaluation of Doxorubicin and Paclitaxel-Loaded Pluronic Micelles Decorated with c(RGDyK) Peptide, *PLoS One*, 2016, **11**(3), e0149952, DOI: **10.1371/journal.pone.0149952**.

42 B. Shi, C. Fang, M. X. You, Y. Zhang, S. Fu and Y. Pei, Stealth MePEG-PCL Micelles: Effects of Polymer Composition on Micelle Physicochemical Characteristics, in Vitro Drug Release, in Vivo Pharmacokinetics in Rats and Biodistribution in S180 Tumor Bearing Mice, *Colloid Polym. Sci.*, 2005, **283**(9), 954–967, DOI: **10.1007/s00396-004-1243-8**.

43 L. W. E. Starmans, M. A. P. M. Hummelink, R. Rossin, E. C. M. Kneepkens, R. Lamerichs, K. Donato, K. Nicolay and H. Grüll, ^{89}Zr- and Fe-Labeled Polymeric Micelles for Dual Modality PET and T_1-Weighted MR Imaging, *Adv. Healthcare Mater.*, 2015, **4**(14), 2137–2145, DOI: **10.1002/adhm.201500414**.

44 L. Scarfe, N. Brillant, J. D. Kumar, N. Ali, A. Alrumayh, M. Amali, S. Barbellion, V. Jones, M. Niemeijer, S. Potdevin, G. Roussignol, A. Vaganov, I. Barbaric, M. Barrow, N. C. Burton, J. Connell, F. Dazzi, J. Edsbagge, N. S. French, J. Holder, C. Hutchinson, D. R. Jones, T. Kalber, C. Lovatt, M. F. Lythgoe, S. Patel, P. S. Patrick, J. Piner, J. Reinhardt, E. Ricci, J. Sidaway, G. N. Stacey, P. J. Starkey Lewis, G. Sullivan, A. Taylor, B. Wilm, H. Poptani, P. Murray, C. E. P. Goldring and B. K. Park, Preclinical Imaging Methods for Assessing the Safety and Efficacy of Regenerative Medicine Therapies, *npj Regener. Med.*, 2017, **2**(1), 28, DOI: **10.1038/s41536-017-0029-9**.

45 S. C. Owen, D. P. Y. Chan and M. S. Shoichet, Polymeric Micelle Stability, *Nano Today*, 2012, **7**(1), 53–65, DOI: **10.1016/j.nantod.2012.01.002**.

46 A. Berger, Positron Emission Tomography, *Br. Med. J.*, 2003, **326**(7404), 1449–1449, DOI: **10.1136/bmj.326.7404.1449**.

47 F. Costamagna, H. Hillaireau, J. Vergnaud, D. Clarisse, L. Jamgotchian, O. Loreau, S. Denis, E. Gravel, E. Doris and E. Fattal, Nanotoxicology at the Particle/Micelle Frontier: Influence of Core-Polymerization on the Intracellular Distribution, Cytotoxicity and Genotoxicity of Polydiacetylene Micelles, *Nanoscale*, 2020, **12**(4), 2452–2463, DOI: **10.1039/c9nr08714a**.

48 S. D. Perrault, C. Walkey, T. Jennings, H. C. Fischer and W. C. W. Chan, Mediating Tumor Targeting Efficiency of Nanoparticles through Design, *Nano Lett.*, 2009, **9**(5), 1909–1915, DOI: **10.1021/nl900031y**.

49 D. R. Rice, A. G. White, W. M. Leevy and B. D. Smith, Fluorescence Imaging of Interscapular Brown Adipose Tissue in Living Mice, *J. Mater. Chem. B*, 2015, **3**(9), 1979–1989, DOI: **10.1039/C4TB01914H**.

50 D. S. Abou, T. Ku and P. M. Smith-Jones, In Vivo Biodistribution and Accumulation of 89Zr in Mice, *Nucl. Med. Biol.*, 2011, **38**(5), 675–681, DOI: **10.1016/j.nucmedbio.2010.12.011**.

51 G. W. Severin, J. T. Jørgensen, S. Wiehr, A.-M. Rolle, A. E. Hansen, A. Maurer, M. Hasenberg, B. Pichler, A. Kjær and A. I. Jensen, The Impact of Weakly Bound 89Zr on Preclinical Studies: Non-Specific Accumulation in Solid Tumors and Aspergillus Infection, *Nucl. Med. Biol.*, 2015, **42**(4), 360–368, DOI: **10.1016/j.nucmedbio.2014.11.005**.

52 D. S. Abou, D. L. J. Thorek, N. N. Ramos, M. W. H. Pinkse, H. T. Wolterbeek, S. D. Carlin, B. J. Beattie and J. S. Lewis, 89Zr-Labeled Paramagnetic Octreotide-Liposomes for PET-MR Imaging of Cancer, *Pharm. Res.*, 2013, **30**(3), 878–888, DOI: **10.1007/s11095-012-0929-8**.

53 Y. Zhang, R. Lin, H. Li, W. He, J. Du and J. Wang, Strategies to Improve Tumor Penetration of Nanomedicines through Nanoparticle Design, *Wiley Interdiscip. Rev.: Nanomed. Nanobiotechnol.*, 2019, **11**(1), DOI: **10.1002/wnan.1519**.

54 H. Cabral, Y. Matsumoto, K. Mizuno, Q. Chen, M. Murakami, M. Kimura, Y. Terada, M. R. Kano, K. Miyazono, M. Uesaka, N. Nishiyama and K. Kataoka, Accumulation of Sub-100 Nm Polymeric Micelles in Poorly Permeable Tumours Depends on Size, *Nat. Nanotechnol.*, 2011, **6**(12), 815–823, DOI: **10.1038/nnano.2011.166**.

55 J.-M. Escoffre, A. Novell, S. Serrière, T. Lecomte and A. Bouakaz, Irinotecan Delivery by Microbubble-Assisted Ultrasound: *In Vitro* Validation and a Pilot Preclinical Study, *Mol. Pharmaceutics*, 2013, **10**(7), 2667–2675, DOI: **10.1021/mp400081b**.

56 J.-M. Escoffre, A. Zeghimi, A. Novell and A. Bouakaz, *In vivo* Gene Delivery by Sonoporation: Recent Progress and Prospects, *Curr. Gene Ther.*, 2012, **13**(1), 2–14, DOI: **10.2174/1566523211313010002**.